Radiotherapy and Oncology 182 (2023) 109506

Contents lists available at ScienceDirect

Radiotherapy and Oncology

journal homepage: www.thegreenjournal.com

Original Article

Feasibility of delivered dose reconstruction for MR-guided SBRT of pancreatic tumors with fast, real-time 3D cine MRI

Guus Grimbergen [a,*], Giulia G. Pötgens [b], Hidde Eijkelenkamp [a], Bas W. Raaymakers [a], Martijn P.W. Intven [a], Gert J. Meijer [a]

[a] Department of Radiation Oncology, University Medical Center Utrecht; and [b] Department of Biomedical Engineering, Eindhoven University of Technology, the Netherlands

ARTICLE INFO

Article history:
Received 22 November 2022
Received in revised form 24 January 2023
Accepted 25 January 2023
Available online 2 February 2023

Keywords:
Pancreatic cancer
MR-guided SBRT
Intrafraction motion
Dose reconstruction
3D cine MRI

ABSTRACT

Background and purpose: In MR-guided SBRT of pancreatic cancer, intrafraction motion is typically monitored with (interleaved) 2D cine MRI. However, tumor surroundings are often not fully captured in these images, and motion might be distorted by through-plane movement. In this study, the feasibility of highly accelerated 3D cine MRI to reconstruct the delivered dose during MR-guided SBRT was assessed.
Materials and methods: A 3D cine MRI sequence was developed for fast, time-resolved 4D imaging, featuring a low spatial resolution that allows for rapid volumetric imaging at 430 ms. The 3D cines were acquired during the entire beam-on time of 23 fractions of online adaptive MR-guided SBRT for pancreatic tumors on a 1.5 T MR-Linac. A 3D deformation vector field (DVF) was extracted for every cine dynamic using deformable image registration. Next, these DVFs were used to warp the partial dose delivered in the time interval between consecutive cine acquisitions. The warped dose plans were summed to obtain a total delivered dose. The delivered dose was also calculated under various motion correction strategies. Key DVH parameters of the GTV, duodenum, small bowel and stomach were extracted from the delivered dose and compared to the planned dose. The uncertainty of the calculated DVFs was determined with the inverse consistency error (ICE) in the high-dose regions.
Results: The mean (SD) relative (ratio delivered/planned) $D_{99\%}$ of the GTV was 0.94 (0.06), and the mean (SD) relative $D_{0.5cc}$ of the duodenum, small bowel, and stomach were respectively 0.98 (0.04), 1.00 (0.07), and 0.98 (0.06). In the fractions with the lowest delivered tumor coverage, it was found that significant lateral drifts had occurred. The DVFs used for dose warping had a low uncertainty with a mean (SD) ICE of 0.65 (0.07) mm.
Conclusion: We employed a fast, real-time 3D cine MRI sequence for dose reconstruction in the upper abdomen, and demonstrated that accurate DVFs, acquired directly from these images, can be used for dose warping. The reconstructed delivered dose showed only a modest degradation of tumor coverage, mostly attainable to baseline drifts. This emphasizes the need for motion monitoring and development of intrafraction treatment adaptation solutions, such as baseline drift corrections.

Stereotactic body radiotherapy (SBRT) has been established as a feasible therapy for unresectable tumors in and around the pancreas [1–6]. MR-guided radiotherapy [7,8] has enabled effective SBRT for this tumor site, with safe delivery of high irradiation doses in hypofractionated regimens, because of its excellent online imaging capabilities compared to its conventional, CT-guided counterparts [9].

MR-guided radiotherapy also enables simultaneous imaging during treatment delivery, for e.g. intrafraction motion monitoring and retrospective treatment evaluation. This feature is especially important for SBRT in the upper abdomen, because of the proximity of these tumors to highly radiosensitive organs at risk (OARs) and potentially large motion amplitudes. Mitigating respiratory motion with passive motion management, like abdominal compression, is a well-established method in the upper abdomen [10–16], but residual motion and small drifts can still have a significant dosimetric impact on target coverage and OAR dose [17–20].

Online motion monitoring in the upper abdomen is challenging due to the limitations of contemporary MRI techniques. In order to capture detrimental breathing irregularities and tumor drifts, imaging ideally needs to be conducted in a time-resolved fashion, at a frequency fast enough to capture respiratory motion. In current practice, this is mainly achieved with 2D cine MRI, which was employed in a previous study to perform delivered dose

* Corresponding author at: Department of Radiation Oncology, University Medical Center Utrecht, Heidelberglaan 100, 3584CX Utrecht, the Netherlands.
E-mail address: g.grimbergen@umcutrecht.nl (G. Grimbergen).

https://doi.org/10.1016/j.radonc.2023.109506
0167-8140/

reconstruction in the upper abdomen [20]. However, this technique suffers from limited field-of-view (FOV), being unable to capture tissue motion outside the 2D plane(s), and is unsuitable for assessing out-of-plane motion. Attempts to design time-resolved volumetric acquisitions were often focused on reconstructing 3D motion from 2D cine MRI [21–26]. However, high-frequency, time-resolved 4D MRI is also possible through direct acquisition when reducing the spatial resolution of the acquired images [27]. This technique results in a lower visual image quality, but modern deformable image registration algorithms can still extract accurate 3D motion information at large voxel sizes [28,29]. Moreover, assuming that the motion fields vary slowly in the spatial domain, they can be upsampled and interpolated to different coordinate grids with higher resolutions. This way, low-resolution, real-time 3D cine MRI becomes a potential technique for dose reconstruction in the upper abdomen.

In this study, we aimed to investigate the use of highly accelerated 3D cine MRI for reconstruction of the delivered dose during MR-guided SBRT of pancreatic tumors, and analyze the volumetric motion patterns extracted from these 3D cine MRIs. In addition, the delivered dose was calculated under various simulated motion correction strategies.

Materials & methods

Patient and treatment overview

Five patients were included that underwent online adaptive MR-guided SBRT for upper abdominal malignancies between August and September 2022. Patients provided informed consent through the prospective Multi-OutcoMe EvaluatioN of radiation Therapy Using the MR-linac (MOMENTUM) study (NCT04075305). Patient characteristics are given in Table 1.

The patients were treated with a 5x8 Gy SBRT regimen on the Elekta Unity (Elekta AB, Stockholm, Sweden) magnetic resonance linear accelerator (MR-Linac), a 7 MV flatting filter free (FFF) linear accelerator combined with a 1.5 T wide bore MRI scanner. Treatment was conducted in an online adaptive fashion [30], in which the treatment plan was adapted to a 3D T_2w MRI sequence acquired at the start of each fraction. Intrafraction tumor motion was mitigated by compression with an abdominal corset [11,16]. The treatment protocol did not include bowel preparation. An isotropic planning target volume (PTV) margin of 3 mm was used, and treatment was delivered with a 9–14 beam step-and-shoot intensity-modulated radiotherapy (IMRT) technique. Our institutional planning objectives and constraints are given in supplementary Table S1.

Imaging overview

A 3D cine MRI sequence was developed for fast, time-resolved 4D imaging. The sequence is an RF-spoiled, T_1-weighted, gradient echo scan with a low resolution of $5 \times 5 \times 6$ mm^3 voxel size. The low resolution allows for high-speed volumetric imaging at 2.3 Hz (430 ms per volume) when combined with acceleration strategies such as compressed SENSE [31,32], partial Fourier, and a large echo train length. The water-fat shift was manually set to a maximum of 0.5 mm, to ensure geometrically accurate images. The sequence was tuned using the standard parameters available in the clinical environment of the MR-Linac, such that this sequence can be readily implemented on similar systems. The 3D cine MRIs were acquired during the entire beam-on time of each fraction. A detailed overview of the sequence parameters is given in Table 2.

Dose reconstruction

The reconstruction of the delivered dose was conducted in a time-resolved fashion, where the total dose plan was split into partial doses for every cine dynamic. This way, the motion measured in a cine dynamic was only applied to the dose that was delivered during that particular dynamic's acquisition time. This was done by using the machine log files of the linac, which log the current state of the linac (gantry angle, dose rate, and multi-leaf collimator positions) during treatment delivery every 40 ms. Because the entries in these log files are timestamped with the current clock time, they can be segmented into partial logs based on the acquisition times of every cine dynamic. When combined with a pseudo-CT (bulk electron density assignment of the pre MRI: bone = 1.117 g/cm^3, air = 0.001 g/cm^3, all other tissue was assigned as water = 1.000 g/cm^3), a partial dose plan can be calculated with GPUMCD [33] for every cine dynamic. Motion was extracted from the 3D cine MRIs as deformation vector fields (DVFs) using EVolution [34] ($\alpha = 0.35$, patch size = $5 \times 5 \times 5$). The cine dynamics were internally registered; therefore, the DVFs relate the motion of each incoming dynamic to a reference state. In order to later apply the DVFs to the partial dose plans, this reference state needs to correspond to the anatomical state for which the dose plan was created, assumed to be the time-weighted average position of the internal anatomy. To create an appropriate reference cine dynamic, a first registration loop was run in which the first 30 seconds of cine MRI data was registered to a dynamic in the exhale state. Then, the average DVF over this period was calculated and used to warp this exhale dynamic to create a new dynamic, corresponding to the time-weighted average position. This dynamic was used as the reference image during the main registration loop.

After every registration of the reference dynamic to an incoming cine dynamic, the resulting 3D DVF was interpolated to the coordinate grid of the partial dose plans (voxel size: $3 \times 3 \times 3$ mm^3). A cubic interpolation method was used to preserve large motion gradients between stationary and mobile tissue, for example at the spine interface. After interpolation, the partial dose plan corresponding to the incoming dynamic was warped while preserving energy/mass transfer [35], taking the density changes into account during dose warping. The partial dose plans were summed with and without warping, resulting in the delivered and planned dose, respectively. The method for dose reconstruction is illustrated in Fig. 1. After warping a partial dose plan, the same DVF was used to warp the GTV contour from the reference state to the incoming dynamic. This was done to create a GTV contour that moved along with the anatomy, of which the center of mass could be tracked to generate a 3D motion trace of

Table 1
Patient characteristics.

#	Age	Sex	GTV/PTV volume (cm^3)	Diagnosis	Tumor location
1	71	M	23/38	Locally advanced pancreatic carcinoma	Head
2	73	F	144/202	Locally advanced pancreatic carcinoma	Tail
3	59	M	47/81	Locally recurrent pancreatic carcinoma	Tail
4	72	M	2/5	Pancreatic neuroendocrine carcinoma	Tail
5	61	M	5/11	Pancreatic oligometastasis of renal cell carcinoma	Head

Table 2
3D cine MRI sequence parameters.

Parameter	Value
Scanning technique	RF-spoiled Fast Field Echo
FOV (mm^3)	400 × 400 × 180
Acquisition/reconstruction voxel size (mm^3)	5 × 5 × 6
TE/TR (ms)	1.1/2.2
FA (°)	10
Compressed SENSE factor	4
Partial Fourier factor	0.7 (*x*-*y*), 0.7 (*y*-*z*)
Echo train length	185
Readout bandwidth (Hz/pixel)	2170
Scan type per dynamic (s)	0.430

the tumor. This motion trace was characterized by its respiratory motion amplitude and maximum drift in the same manner as in our previous studies [16,20]. The respiratory amplitude was calculated by high-pass filtering the motion trace and calculating the peak-to-peak distance, and the drift magnitude was calculated by low-pass filtering and extracting the maximum absolute value of the drift motion. The overall respiratory amplitude and drift were calculated as the 2-norm of their values in the three cardinal directions: cranio-caudal (*CC*), anterior-posterior (*AP*), and left–right (*LR*).

Motion correction simulation

The above method for dose reconstruction and GTV motion monitoring was also used to simulate various intrafraction motion correction strategies, and calculate their subsequent impact on the delivered dose in terms of tumor coverage.

Three strategies were simulated, using the measured GTV motion trace to apply a beam isocenter shift as a 3D offset to the DVFs before warping the dose. The first strategy was a thresholded baseline shift, where the beam isocenter is set to the moving average tumor position over the last 30 seconds, when this average position exceeds a certain distance threshold from the previous isocenter. Smaller thresholds will lead to better conformity but might require corrections at an unfeasibly high frequency, as each correction would realistically require a minimum processing time. Therefore, six different thresholds were investigated: 0.5, 1.0, 1.5, 2.0, 2.5 and 3.0 mm. The second strategy was tumor trailing [36], where the isocenter is *continuously* updated with the average tumor position. Trailing can be regarded as a thresholded baseline shift with a threshold of 0 mm. The third strategy was tumor tracking, where the applied offset is continuously updated with the actual tumor position.

Evaluation

For delivered dose evaluation, key DVH parameters of the GTV and neighboring OARs (duodenum, small bowel, stomach) were extracted and compared to their respective values of the planned dose, expressed as the ratio between the delivered dose over the planned dose. For the gross tumor volume (GTV), the $D_{99\%}$ was evaluated, and for the OARs the $D_{0.5cc}$.

When performing 3D deformable image registration to warp dose maps, it is important to ensure that the obtained motion is realistic up to a dosimetrically relevant level. This is a notoriously complicated problem in the absence of a ground truth. We therefore employed the inverse consistency error (ICE) as a metric to evaluate the quality of the obtained DVFs [37,38], which can also be applied to low-resolution DVF evaluation [27]. Moreover, this inverse consistency is a commonly used evaluation metric in dose warping studies, as it measures spatial uncertainty of the warped dose on a voxel-by-voxel basis [39–42]. A DVF is known to be inverse consistent when a voxel at reference location $\vec{r}_0$, mapped to location $\vec{r}_t$ with $\mathrm{DVF}_{I_0 \to I_t}$, ends up back at $\vec{r}_0$ when the inverse $\mathrm{DVF}_{I_t \to I_0}$ is applied to $\vec{r}_t$. If instead it is mapped at a different location $\vec{r}'_0$, the ICE is equal to $\|\vec{r}'_0 - \vec{r}_0\|_2$ (see Fig. 2).

The ICE was calculated for the first two minutes of 3D cine MRI data of every fraction, and evaluated in only the dosimetrically relevant area where voxel values in the planned dose were above 20 Gy (scaled to the complete 40 Gy treatment regimen).

Results

All five patients received complete treatment of five fractions. However, in one fraction the 3D cine acquisition was started too late after beam-on, and in another fraction, the linac log file was

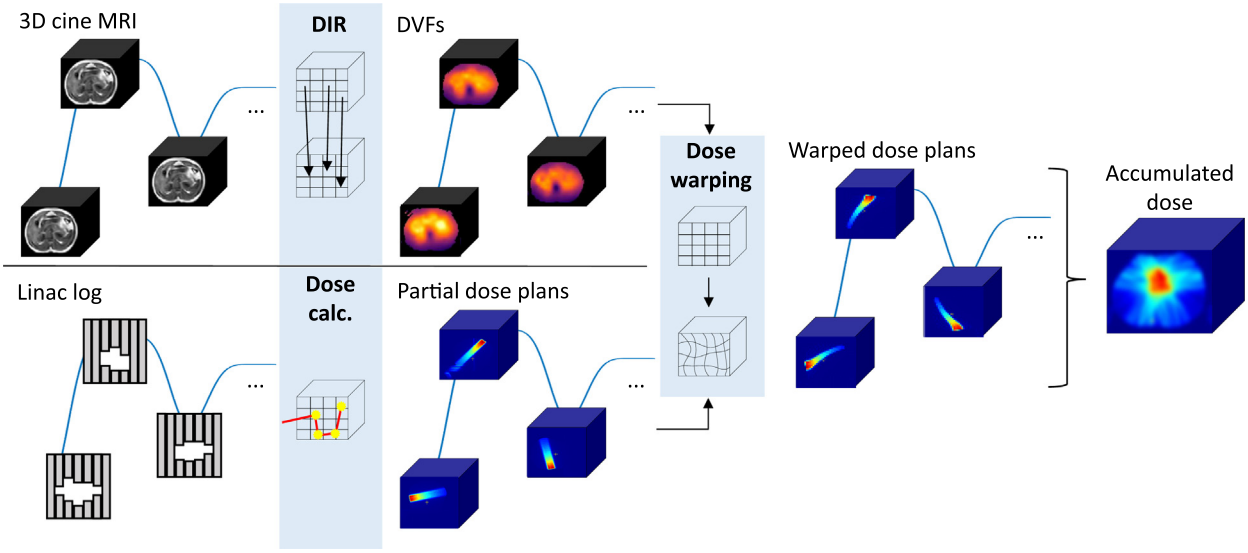

Fig. 1. The method pipeline. 3D cines are acquired every 430 ms during beam-on, and for each dynamic the current state of the linac is saved and reconstructed into a partial dose plan. Deformable image registration (DIR) is performed on the cine frames, and the resulting deformation vector field (DVF) is used to warp the corresponding partial dose plan. The warped doses are then summed to obtain the delivered dose.

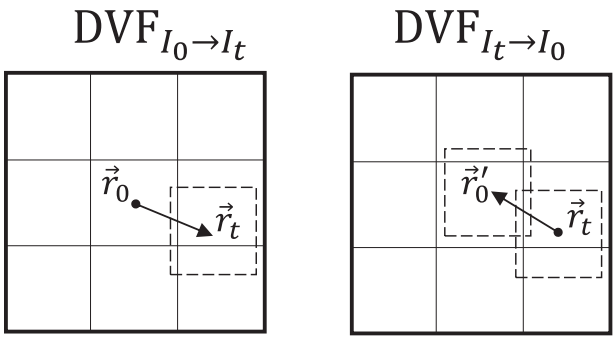

Fig. 2. Schematic representation of the inverse consistency error (ICE). After registering reference image I_0 to incoming image I_t, the resulting DVF maps voxel $\vec{r_0}$ to$\vec{r_t}$. The inverse DVF, obtained by registering I_t to I_0, maps $\vec{r_0}$ back to $\vec{r_0'}$. If inaccuracies in the registration occur, this location might differ from the starting position. The ICE is defined as the length of the difference vector between $\vec{r_0'}$ and$\vec{r_0}$. Note that $\vec{r_t}$ often does not fall exactly on the image grid, so the inverse DVF needs to be interpolated to obtain the backward vector at that location.

missing. Therefore, the data from these fractions was disregarded, and a total of 23 fractions was included in the final analysis.

A 3D cine MRI acquisition demo is given in supplementary video 1 (top row), along with the corresponding motion-compensated dynamics (bottom row). In the latter, the 3D deformable image registration quality can be assessed by the level of residual motion present in the images. Please note that this video is not a real-time representation but sped up for visual purposes to ten dynamics per second, covering 64 seconds of actual cine MRI acquisition. Quantitatively, a high inverse consistency was achieved in the high-dose region, with a mean (SD) ICE of 0.65 (0.07) mm over all fractions. An example of an ICE map is given in supplementary Fig. S1. Upon closer inspection of the obtained motion fields, the motion gradient at the spinal interface turned out less steep than initially inspected, so the cubic interpolation method did not result in different motion fields than with linear interpolation (supplementary Fig. S2).

The relative (ratio delivered/planned) DVH parameters of the GTV, duodenum, small bowel, and stomach are presented in Fig. 3, with respect to the measured GTV respiratory amplitude and drift magnitude. The mean (SD) relative $D_{99\%}$ of the GTV was 0.94 (0.06), and the mean (SD) relative $D_{0.5cc}$ of the duodenum, small bowel, and stomach were respectively 0.98 (0.04), 1.00 (0.07), and 0.98 (0.06). Upon closer inspection of the fractions where the largest decline in tumor coverage was measured, it was observed that significant lateral drifts had occurred during these fractions. An example is given in supplementary video 2, where the 3D cine MRI and GTV motion trace can be seen of a fraction where the delivered GTV $D_{99\%}$ was 88 % of the planned $D_{99\%}$. The video, played in real-time, features a bulk shift about two-thirds into the treatment as the patient repositioned themselves 6.5 millimeters to their right. One minute and 40 seconds later, the patient shifted back to roughly the baseline position. Another example is the fraction with the lowest relative GTV $D_{99\%}$, which was 76 % of the planned $D_{99\%}$. The GTV motion trace is given in supplementary Fig. S3. In this fraction, the lateral drift was smaller than in the previous example, but it occurred relatively early into treatment and sustained for almost the entire beam-on time. It had, therefore, a larger detrimental effect on tumor coverage. This same fraction also featured the largest relative OAR dose increase of 122 % in small bowel $D_{0.5cc}$.

In the motion correction simulations, it was found that thresholded baseline shifts already greatly mitigate the dosimetric effects of all the intrafraction motion during the beam-on time, similar to the continuous trailing strategy (Fig. 4). Tracking strategies further improved the congruence between planned and delivered dose. However, the effects of tracking the respiratory motion turned out to be limited for this cohort. For the different threshold values, the average number of corrections per fraction was: 47 for 0.5 mm, 16 for 1.0 mm, 7 for 1.5 mm, 4 for 2.0 mm, 2 for 2.5 mm and 1 for 3.0 mm. Further improvement in target coverage was limited when using lower thresholds or continuous trailing.

Discussion

We have employed a fast, real-time 3D cine MRI sequence for delivered dose reconstruction, using deformable image registration to obtain highly accelerated volumetric motion information directly from the acquired images. In this study, we have demonstrated that these motion fields can be used for dose warping to reconstruct the delivered dose for MR-guided SBRT of upper abdominal tumors.

In its current retrospective setting, we believe that the most useful clinical application of the end-to-end dose reconstruction method would be as a QA tool for offline treatment evaluation, after a fraction has been delivered. Should the delivered dose show that unfavorable deviations have occurred in tumor coverage or OAR dose, the treatment strategy of the upcoming fractions might be adapted to "repair" tumor cold spots and/or mitigate OAR hot spots.

The results from the delivered dose reconstructions showed in most fractions modest dosimetric degradations caused by intrafraction motion. However, in some fractions tumor coverage was clearly impacted by intrafraction drifts during bream-on time. With an average beam-on time of 8 + minutes, there is a realistic probability of these small drifts occurring. The OARs were less impacted by intrafraction motion than the tumor coverage. The largest relative OAR dose increase of 122 % in small bowel $D_{0.5cc}$ turned out to be a negligible absolute increase from 11.8 Gy to 14.3 Gy (scaled to the complete 40 Gy treatment regimen). In only two fractions, the delivered dose violated the OAR dose constraints, and in both these cases this violation was already present in the

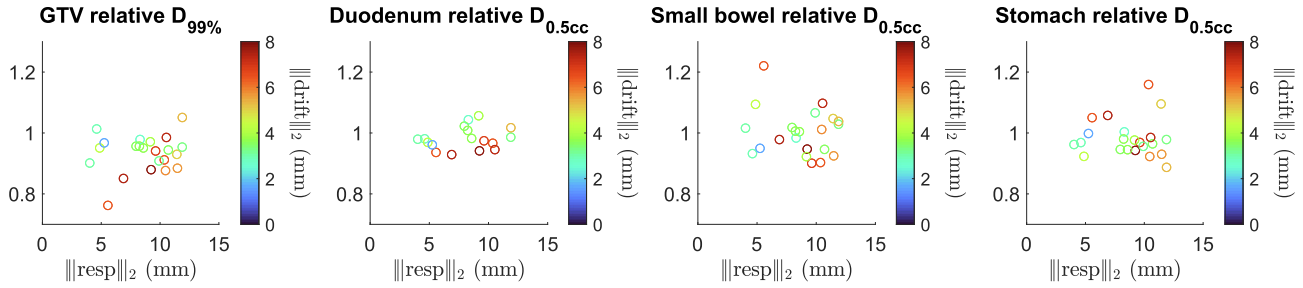

Fig. 3. The relative (ratio delivered/planned) DVH parameters in the GTV and OARs of the measured intrafraction motion. Each point represents a fraction, accumulated with the motion measured during that fraction, and characterized by the magnitudes of the respiratory amplitude (x-axis value) and drift of that fraction (point color scale).

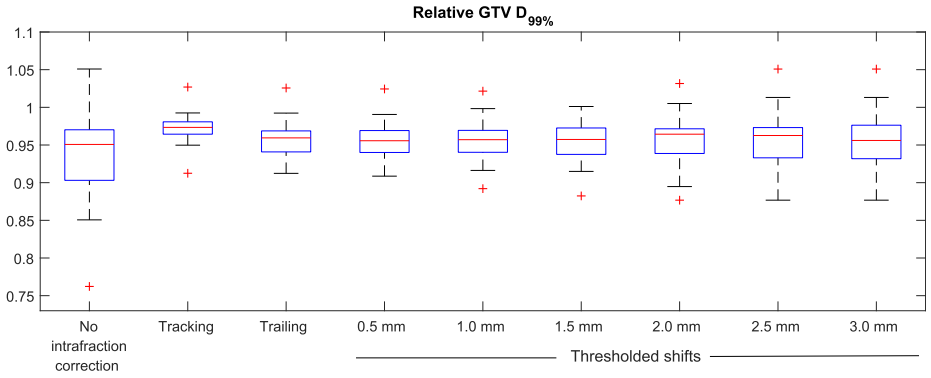

Fig. 4. The simulated effect of tracking, trailing and thresholded baseline shifts on the delivered GTV $D_{99\%}$ for the fractions in this study. The whiskers of the boxplot extend to the minimum and maximum of the values not considered outliers (values further than 1.5 times the interquartile range from the box). The outliers are indicated by the red plus signs.

planned dose. One fraction had a violated stomach constraint in the planned dose, but this was as such mitigated by intrafraction motion that the $D_{0.5cc}$ fell below the constraint in the delivered dose. For further clarification, we have included all absolute OAR $D_{0.5cc}$ values in supplementary Table S2.

The simulations demonstrated that the largest degradations in tumor coverage could be sufficiently improved with systematic monitoring of the target in combination with a correction strategy. Since thresholded baseline shifts require a substantially lower number of intrafraction corrections than continuous trailing or tracking, this strategy might be the most accessible candidate for a clinical solution to mitigate detrimental drifts. The chosen threshold value will depend on how long a correction would take to process and execute in practice. Based on the number of corrections that were applied in the simulations, and assuming a maximum correction frequency of once per minute, a threshold of 1.5 mm (resulting in seven intrafraction corrections on average) would have been the recommended value for this cohort.

The 3D cine MRI sequence was developed as plug-and-play, using acquisition and reconstruction options available in the standard clinical environment of the 1.5 T MR-Linac. Therefore, it also has the potential as a motion monitoring tool comparable to the 2D cine sequences used for gating/tracking on MR-Linac systems. However, mainly due to the high compressed SENSE factor, the reconstruction time (approximately-one second per dynamic) is currently too long for online applications. Nonetheless, with future (GPU-based) acceleration of reconstruction, we believe that time-resolved volumetric sequences will become a feasible method for real-time online motion monitoring, overcoming the limitations of 2D acquisitions. Furthermore, with the particular low-resolution sequence employed in this study, the reduced data size also means that images can be streamed and processed with minimal latency.

A critical workflow component in 3D dose warping is the QA of the obtained motion fields. Because of the low resolution of the 3D cine MRIs much detail is lost, which may introduce additional uncertainty in the DVFs. However, we believe that the motion of upper abdominal tumors and the immediate surroundings in the high dose area (such as abutting OARs), are predominantly characterized by rigid transformations, especially when restricted by abdominal compression. This holds both for the respiratory motion and for bulk shifts. Because of their geometric simplicity, these rigid displacements can typically be easily captured by DIR algorithms. There might still be a deformable component present which may be harder to accurately extract under low resolutions, for example the digestive motion of surrounding bowel structures. Bowel motion can be quite subtle and might require imaging with e.g. higher contrast, higher resolution or oral contrast agents [43–46]. However, this motion in the immediate vicinity of the tumor, as well as the deformable motion component of the tumor itself is much smaller than the rigid component, often periodic and therefore might be less dosimetrically relevant.

While this study only employed a single DVF uncertainty metric and lacks a ground truth for true error quantification, the mean ICE of 0.65 mm in the high-dose region still signifies a low uncertainty in the obtained motion fields. Moreover, this study was confined to a relatively simple problem within the context of dose warping studies; image registration was performed in a highly correlated set of images and produced spatially smooth, low-resolution 3D motion fields reflecting only global anatomical motion. Even though it requires more sophisticated imaging tools, we argue that intrafraction image registration and dose warping is less error-prone than *inter*fraction dose accumulation, where motion fields need to reflect much more dramatic anatomy changes, as structures are likely to grow, shrink, appear and disappear between consecutive images [47]. Nevertheless, uncertainty in the obtained motion fields will still lead to nontrivial uncertainty in the reconstructed dose plans. Quantifying the uncertainty in dose accumulation is a known and open problem in the field [48–54], and while considered beyond the scope of this study, it should be a vital part of the clinical implementation of any intrafraction dose accumulation method, if clinical decision making is going to be based on the resulting delivered dose reconstructions.

Conclusion

This study showed that highly accelerated 3D cine MRI during beam-on can be used for delivered dose reconstruction during MR-guided SBRT of pancreatic tumors. The low-resolution cine dynamics can be deformably registered with substantial inverse consistency. This study's results show that drifts are the most detrimental motion components for adequate tumor coverage in the upper abdomen. However, these errors can be resolved through simple online correction strategies, such as intrafraction baseline shift corrections. Moreover, our method would allow day-to-day treatment evaluation to optimize the treatment strategy of the upcoming fractions.

Declaration of Competing Interest

The authors declare that they have no known competing financial interests or personal relationships that could have appeared to influence the work reported in this paper.

Acknowledgments

The authors would like to thank Lando Bosma and Cornel Zachiu for the fruitful discussions. This work was supported by the Dutch Cancer Foundation (KWF) under Grant Agreement no. 12665.

Appendix A. Supplementary material

Supplementary data to this article can be found online at https://doi.org/10.1016/j.radonc.2023.109506.

References

[1] Chang DT, Schellenberg D, Shen J, Kim J, Goodman KA, Fisher GA, et al. Stereotactic radiotherapy for unresectable adenocarcinoma of the pancreas. Cancer 2009;115:665–72. https://doi.org/10.1002/cncr.24059.
[2] Mahadevan A, Jain S, Goldstein M, Miksad R, Pleskow D, Sawhney M, et al. Stereotactic body radiotherapy and gemcitabine for locally advanced pancreatic cancer. Int J Radiat Oncol Biol Phys 2010;78:735–42. https://doi.org/10.1016/j.ijrobp.2009.08.046.
[3] Heerkens HD, Van Vulpen M, Erickson B, Reerink O, Intven MPW, van den Berg CAT, et al. MRI guided stereotactic radiotherapy for locally advanced pancreatic cancer. Br J Radiol 2018;91:20170563. https://doi.org/10.1259/bjr.20170563.
[4] Rudra S, Jiang N, Rosenberg SA, Olsen JR, Roach MC, Wan L, et al. Using adaptive magnetic resonance image-guided radiation therapy for treatment of inoperable pancreatic cancer. Cancer Med 2019;8:2123–32. https://doi.org/10.1002/cam4.2100.
[5] Reyngold M, Parikh P, Crane CH. Ablative radiation therapy for locally advanced pancreatic cancer: techniques and results. Radiat Oncol 2019;14:1–8. https://doi.org/10.1186/s13014-019-1309-x.
[6] Tringale KR, Tyagi N, Reyngold M, Romesser PB, Wu A, O'Reilly EM, et al. Stereotactic ablative radiation for pancreatic cancer on a 1.5 tesla magnetic resonance-linac system. Phys Imaging Radiat Oncol 2022;24:88–94. https://doi.org/10.1016/j.phro.2022.10.003.
[7] Mutic S, Dempsey JF. The ViewRay system: magnetic resonance–guided and controlled radiotherapy. Semin Radiat Oncol 2014;24:196–9. https://doi.org/10.1016/j.semradonc.2014.02.008.
[8] Raaymakers BW, Jürgenliemk-Schulz IM, Bol GH, Glitzner M, Kotte ANTJ, Van Asselen B, et al. First patients treated with a 1.5 T MRI-Linac: clinical proof of concept of a high-precision, high-field MRI guided radiotherapy treatment. Phys Med Biol 2017;62:L41. https://doi.org/10.1088/1361-6560/aa9517.
[9] Placidi L, Romano A, Chiloiro G, Cusumano D, Boldrini L, Cellini F, et al. On-line adaptive MR guided radiotherapy for locally advanced pancreatic cancer: clinical and dosimetric considerations. Tech Innov Patient Support Radiat Oncol 2020;15:15–21. https://doi.org/10.1016/j.tipsro.2020.06.001.
[10] Lovelock DM, Zatcky J, Goodman K, Yamada Y. The effectiveness of a pneumatic compression belt in reducing respiratory motion of abdominal tumors in patients undergoing stereotactic body radiotherapy. Technol Cancer Res Treat 2014;13:259–67. https://doi.org/10.7785/tcrt.2012.500379.
[11] Heerkens HD, Reerink O, Intven MPW, Hiensch RR, Van Den Berg CAT, Crijns SPM, et al. Pancreatic tumor motion reduction by use of a custom abdominal corset. Phys Imaging Radiat Oncol 2017;2:7–10. https://doi.org/10.1016/j.phro.2017.02.003.
[12] Campbell WG, Jones BL, Schefter T, Goodman KA, Miften M. An evaluation of motion mitigation techniques for pancreatic SBRT. Radiother Oncol 2017;124:168–73. https://doi.org/10.1016/j.radonc.2017.05.013.
[13] Dolde K, Schneider S, Stefanowicz S, Alimusaj M, Flügel B, Saito N, et al. Comparison of pancreatic respiratory motion management with three abdominal corsets for particle radiation therapy: case study. J Appl Clin Med Phys 2019;20:111–9. https://doi.org/10.1002/acm2.12613.
[14] Fujimoto K, Shiinoki T, Yuasa Y, Onizuka R, Yamane M. Evaluation of the effects of motion mitigation strategies on respiration-induced motion in each pancreatic region using cine-magnetic resonance imaging. J Appl Clin Med Phys 2019;20:42–50. https://doi.org/10.1002/acm2.12693.
[15] Tyagi, N., Liang, J., Burleson, S., Subashi, E., Scripes, P. G., Tringale, K. R., Romesser, P. B., Reyngold, M., and Crane, C. H. Feasibility of ablative stereotactic body radiation therapy of pancreas cancer patients on a 1.5 Tesla magnetic resonance-linac system using abdominal compression. *Phys. Imaging Radiat. Oncol.*, 19:53–59, 2021. doi:10.1016/j.phro.2021.07.006.
[16] Grimbergen G, Eijkelenkamp H, Heerkens HD, Raaymakers BW, Intven MPW, Meijer GJ. Intrafraction pancreatic tumor motion patterns during ungated magnetic resonance guided radiotherapy with an abdominal corset. Phys Imaging Radiat Oncol 2022;21:1–5. https://doi.org/10.1016/j.phro.2021.12.001.
[17] Cusumano D, Dhont J, Boldrini L, Chiloiro G, Teodoli S, Massaccesi M, et al. Predicting tumour motion during the whole radiotherapy treatment: a systematic approach for thoracic and abdominal lesions based on real time MR. Radiother Oncol 2018;129:456–62. https://doi.org/10.1016/j.radonc.2018.07.025.
[18] Dhont J, Vandemeulebroucke J, Burghelea M, Poels K, Depuydt T, Van Den Begin R, et al. The long-and short-term variability of breathing induced tumor motion in lung and liver over the course of a radiotherapy treatment. Radiother Oncol 2018;126:339–46. https://doi.org/10.1016/j.radonc.2017.09.001.
[19] Cusumano D, Dhont J, Boldrini L, Chiloiro G, Romano A, Votta C, et al. Reliability of ITV approach to varying treatment fraction time: a retrospective analysis based on 2D cine MR images. Radiat Oncol 2020;15:1–9. https://doi.org/10.1186/s13014-020-01530-6.
[20] Grimbergen G, Eijkelenkamp H, Heerkens HD, Raaymakers BW, Intven MP, Meijer GJ. Dosimetric impact of intrafraction motion under abdominal compression during MR-guided SBRT for (peri-) pancreatic tumors. Phys Med Biol 2022;67:. https://doi.org/10.1088/1361-6560/ac8ddd185016.
[21] Stemkens B, Tijssen RHN, de Senneville BD, Heerkens HD, Van Vulpen M, Lagendijk JJW, et al. Optimizing 4-dimensional magnetic resonance imaging data sampling for respiratory motion analysis of pancreatic tumors. Int J Radiat Oncol Biol Phys 2015;91:571–8. https://doi.org/10.1016/j.ijrobp.2014.10.050.
[22] Stemkens B, Paulson ES, Tijssen RHN. Nuts and bolts of 4D-MRI for radiotherapy. Phys Med Biol 2018;63:21TR01. https://doi.org/10.1088/1361-6560/aae56d.
[23] Paganelli C, Portoso S, Garau N, Meschini G, Via R, Buizza G, et al. Time-resolved volumetric MRI in MRI-guided radiotherapy: an in silico comparative analysis. Phys Med Biol 2019;64:. https://doi.org/10.1088/1361-6560/ab33e5185013.
[24] Li, G., Liu, Y., and Nie, X. Respiratory-correlated (RC) vs. time-resolved (TR) four-dimensional magnetic resonance imaging (4DMRI) for radiotherapy of thoracic and abdominal cancer. *Front. Oncol.*, 9:1024, 2019. doi:10.3389/fonc.2019.01024.
[25] Borman PTS, Bos C, Stemkens B, Moonen CTW, Raaymakers BW, Tijssen RHN. Assessment of 3D motion modeling performance for dose accumulation mapping on the MR-linac by simultaneous multislice MRI. Phys Med Biol 2019;64:. https://doi.org/10.1088/1361-6560/ab13e3095004.
[26] Dasnoy-Sumell D, Aspeel A, Souris K, Macq B. Locally tuned deformation fields combination for 2D cine-MRI-based driving of 3D motion models. Phys Med 2022;94:8–16. https://doi.org/10.1016/j.ejmp.2021.12.010.
[27] Li G, Wei J, Kadbi M, Moody J, Sun A, Zhang S, et al. Novel super-resolution approach to time-resolved volumetric 4-dimensional magnetic resonance imaging with high spatiotemporal resolution for multi-breathing cycle motion assessment. Int J Radiat Oncol Biol Phys 2017;98:454–62. https://doi.org/10.1016/j.ijrobp.2017.02.016.
[28] Glitzner M, De Senneville BD, Lagendijk JJW, Raaymakers BW, Crijns SPM. On-line 3D motion estimation using low resolution MRI. Phys Med Biol 2015;60:N301. https://doi.org/10.1088/0031-9155/60/16/N301.
[29] Bosma L, Zachiu C, Ries M, de Senneville BD, Raaymakers B. Quantitative investigation of dose accumulation errors from intra-fraction motion in MRgRT for prostate cancer. Phys Med Biol 2021;66:. https://doi.org/10.1088/1361-6560/abe02a065002.
[30] Daamen, L. A., de Mol van Otterloo, S. R., van Goor, I. W., Eijkelenkamp, H., Erickson, B. A., Hall, W. A., Heerkens, H. D., Meijer, G. J., Molenaar, I. Q., van Santvoort, H. C., et al. Online adaptive MR-guided stereotactic radiotherapy for unresectable malignancies in the upper abdomen using a 1.5 T MR-linac. *Acta Oncol.*, 61:111–115, 2022. doi:10.1080/0284186X.2021.2012593.
[31] Lustig M, Donoho D, Pauly JM. Sparse MRI: The application of compressed sensing for rapid MR imaging. Magn Reson Med 2007;58:1182–95. https://doi.org/10.1002/mrm.21391.
[32] Lustig M, Donoho DL, Santos JM, Pauly JM. Compressed sensing MRI. IEEE Signal Process Mag 2008;25:72–82. https://doi.org/10.1109/MSP.2007.914728.
[33] Hissoiny S, Raaijmakers AJE, Ozell B, Després P, Raaymakers BW. Fast dose calculation in magnetic fields with GPUMCD. Phys Med Biol 2011;56:5119. https://doi.org/10.1088/0031-9155/56/16/003.
[34] de Senneville BD, Zachiu C, Ries M, Moonen C. EVolution: an edge-based variational method for non-rigid multi-modal image registration. Phys Med Biol 2016;61:7377. https://doi.org/10.1088/0031-9155/61/20/7377.
[35] Li HS, Zhong H, Kim J, Glide-Hurst C, Gulam M, Nurushev TS, et al. Direct dose mapping versus energy/mass transfer mapping for 4D dose accumulation: fundamental differences and dosimetric consequences. Phys Med Biol 2013;59:173. https://doi.org/10.1088/0031-9155/59/1/173.
[36] Fast M, van de Schoot A, van de Lindt T, Carbaat C, van der Heide U, Sonke J-J. Tumor trailing for liver SBRT on the MR-linac. Int J Radiat Oncol Biol Phys 2019;103:468–78. https://doi.org/10.1016/j.ijrobp.2018.09.011.
[37] Christensen GE, Johnson HJ. Consistent image registration. IEEE Trans Med Imaging 2001;20:568–82. https://doi.org/10.1109/42.932742.
[38] Bender ET, Tomé WA. The utilization of consistency metrics for error analysis in deformable image registration. Phys Med Biol 2009;54:5561. https://doi.org/10.1088/0031-9155/54/18/014.
[39] Bender ET, Hardcastle N, Tomé WA. On the dosimetric effect and reduction of inverse consistency and transitivity errors in deformable image registration for dose accumulation. Med Phys 2012;39:272–80. https://doi.org/10.1118/1.3666948.
[40] Varadhan R, Karangelis G, Krishnan K, Hui S. A framework for deformable image registration validation in radiotherapy clinical applications. J Appl Clin Med Phys 2013;14:192–213. https://doi.org/10.1120/jacmp.v14i1.4066.
[41] Veiga C, Lourenço AM, Mouinuddin S, Van Herk M, Modat M, Ourselin S, et al. Toward adaptive radiotherapy for head and neck patients: uncertainties in

dose warping due to the choice of deformable registration algorithm. Med Phys 2015;42:760–9. https://doi.org/10.1118/1.4905050.
[42] Lowther NJ, Marsh SH, Louwe RJ. Quantifying the dose accumulation uncertainty after deformable image registration in head-and-neck radiotherapy. Radiother Oncol 2020;143:117–25. https://doi.org/10.1016/j.radonc.2019.12.009.
[43] Sprengers AMJ, van der Paardt MP, Zijta FM, Caan MWA, Lamerichs RM, Nederveen AJ, et al. Use of continuously MR tagged imaging for automated motion assessment in the abdomen: a feasibility study. J Magn Reson Imaging 2012;36:492–7. https://doi.org/10.1002/jmri.23637.
[44] De Jonge CS, Smout AJ, Nederveen AJ, Stoker J. Evaluation of gastrointestinal motility with MRI: advances, challenges and opportunities. Neurogastroenterol Motil 2018;30:e13257. https://doi.org/10.1111/nmo.13257.
[45] de Jonge CS, Gollifer RM, Nederveen AJ, Atkinson D, Taylor SA, Stoker J, et al. Dynamic MRI for bowel motility imaging—how fast and how long? Br J Radiol 2018;91:20170845. https://doi.org/10.1259/bjr.20170845.
[46] Barten DL, Laan JJ, Nelissen KJ, Visser J, Westerveld H, Bel A, et al. A 3D cine-MRI acquisition technique and image analysis framework to quantify bowel motion demonstrated in gynecological cancer patients. Med Phys 2021;48:3109–19. https://doi.org/10.1002/mp.14851.
[47] Schultheiss TE, Tomé WA, Orton CG. It is not appropriate to "deform" dose along with deformable image registration in adaptive radiotherapy. Med Phys 2012;39:6531–3. https://doi.org/10.1118/1.4722968.
[48] Murphy MJ, Salguero FJ, Siebers JV, Staub D, Vaman C. A method to estimate the effect of deformable image registration uncertainties on daily dose mapping. Med Phys 2012;39:573–80. https://doi.org/10.1118/1.3673772.
[49] Saleh ZH, Apte AP, Sharp GC, Shusharina NP, Wang Y, Veeraraghavan H, et al. The distance discordance metric—a novel approach to quantifying spatial uncertainties in intra-and inter-patient deformable image registration. Phys Med Biol 2014;59:733. https://doi.org/10.1088/0031-9155/59/3/733.
[50] Rigaud B, Simon A, Castelli J, Gobeli M, Ospina Arango J-D, Cazoulat G, et al. Evaluation of deformable image registration methods for dose monitoring in head and neck radiotherapy. Biomed Res Int 2015;2015. https://doi.org/10.1155/2015/726268.
[51] García-Mollá R, de Marco-Blancas N, Bonaque J, Vidueira L, López-Tarjuelo J, Perez-Calatayud J. Validation of a deformable image registration produced by a commercial treatment planning system in head and neck. Phys Med 2015;31:219–23. https://doi.org/10.1016/j.ejmp.2015.01.007.
[52] Nassef M, Simon A, Cazoulat G, Duménil A, Blay C, Lafond C, et al. Quantification of dose uncertainties in cumulated dose estimation compared to planned dose in prostate IMRT. Radiother Oncol 2016;119:129–36. https://doi.org/10.1016/j.radonc.2016.03.007.
[53] Takemura A, Nagano A, Kojima H, Ikeda T, Yokoyama N, Tsukamoto K, et al. An uncertainty metric to evaluate deformation vector fields for dose accumulation in radiotherapy. Phys Imaging Radiat Oncol 2018;6:77–82. https://doi.org/10.1016/j.phro.2018.05.005.
[54] Bohoudi O, Lagerwaard FJ, Bruynzeel AM, Niebuhr NI, Johnen W, Senan S, et al. End-to-end empirical validation of dose accumulation in MRI-guided adaptive radiotherapy for prostate cancer using an anthropomorphic deformable pelvis phantom. Radiother Oncol 2019;141:200–7. https://doi.org/10.1016/j.radonc.2019.09.014.